The Journal of Green Energy and Environmental Engineering

Research Paper

Preparation and properties of bacterial cellulose/aramid nanofiber in-situ composite aerogels

Ursula Le Guin [1], Frank Herbert [2,*]

[1] Department of Neuroscience, The University of Lahore, Lahore, Pakistan
[2] Université Lille Nord de France, Université du Littoral-Côte d'Opale, UMT 08, 62327 Boulogne sur mer, France
*Corresponding author: Herbert577@hotmail.com

Abstract. With the aim of simultaneously reinforcing bacterial cellulose (BC) aerogel and imparting flame resistance, aramid nanofibers (ANF) were introduced as a strengthening phase, and a BC/ANF composite aerogel was fabricated by allowing BC to grow in situ within the ANF matrix. The structure of BC/ANF aerogel was characterized by FTIR, XRD and SEM. Its thermal properties, flame-retardant performance and tensile fracture properties were tested. How the ANF loading (expressed relative to the mass of the BC culture medium throughout this work) influenced the structure and performance of the BC/ANF aerogels was systematically examined. Relative to the neat BC aerogel, the sample containing 5.0% ANF (BC/ANF-5.0%) delivered a tensile strength of 946.13 kPa — 6.42 times higher — together with an elongation at break of 19.61% (a 6.00-fold improvement), a limiting oxygen index raised to 22.38%, a specific surface area enlarged by 42% to 78.2688 m^2 /g, and a thermal conductivity lowered to 0.0352 W/(m·K). These enhancements can be traced to the interfacial interactions between the two constituents: hydrogen bonding between the amide groups of ANF and the hydroxyl groups of BC tightened their mutual adhesion, while the filling and entanglement of ANF throughout the BC fibrillar network brought the two phases close enough for van der Waals attraction to further consolidate the structure, jointly accounting for the superior mechanical behavior. Moreover, the nanoscale integration of ANF with BC suppressed the generation and breakdown of levoglucosan while favoring char formation, which substantially elevated both the thermal stability and the flame retardancy of the composite aerogel.

Keywords: *bacterial cellulose; aramid nanofiber; composite aerogel; in-situ composite; functional materials*

Received on 02 July 2025, Accepted on 05 Nov 2025, Published on 15 Dec 2025

1 Introduction

Bacterial cellulose (BC) belongs to the family of nanocelluloses produced through bacterial biosynthesis [1]. Notable for its exceptional purity and crystallinity, it is also biocompatible and environmentally benign [2]. The distinctive nanofibrillar architecture of BC translates into aerogels that combine minimal density and large specific surface area with remarkable mechanical strength and adsorption capacity [3]. Consequently, BC aerogels hold considerable promise across diverse application areas, spanning thermal insulation [4-5], adsorbents [6], energy storage [7], and biomedical materials[8]. Nevertheless, BC aerogel also has drawbacks such as high brittleness and high flammability. At present, these problems are mainly solved through material modification or composite technology [9-11].

Aramid nanofiber (ANF) is an organic fiber material with high strength, high modulus and favorable thermal stability [12-13]. Compounding it with pre-formed BC can improve the mechanical and thermal stabilities of BC materials [14]. Using a straightforward vacuum-filtration self-assembly route, CHEN et al.[15] obtained ANF-

reinforced BC nanocomposite membranes; relative to pristine BC membranes (36.3 MPa), the tensile strength of the ANF@BC membranes rose to 58.3 MPa — a gain of 61% — confirming the structural reinforcement imparted by ANF. Through a papermaking-like process, YANG et al.[16] produced ANF/BC composite membranes in which the formulation containing 4% ANF (on a BC mass basis) reached a tensile strength of 104.7 MPa, roughly 2.5 times that of the BC membrane alone (41.3 MPa). In a separate study, ZHANG et al.[17] combined in-situ growth with filtration to build a high-performance lithium-ion battery separator from zeolitic imidazolate framework-8@BC (ZIF-8@BC) and ANF; at a ZIF-8@BC-to-ANF mass ratio of 7∶3, the resulting ZIF-8@BC/30% ANF separator displayed a tensile strength of 70.7 MPa, exceeding that of the BC membrane (50.1 MPa) by 41.1%, and it also self-extinguished readily when ignited, thereby enhancing operational safety.

In this paper, ANF was introduced into the liquid culture medium of *Acetobacter xylinum*. BC produced by static culture was homogeneously compounded with ANF. BC in-situ composite ANF (BC/ANF) aerogel was then prepared by solvent exchange and freeze-drying techniques. The influences of different ANF contents on the morphology, structure, thermal performance, flame-retardant performance, thermal insulation performance and tensile performance of BC/ANF aerogel were discussed. It is expected to solve the problems of high brittleness and high flammability of BC aerogel via composite technology and provide references for the preparation of BC-ANF composite aerogels.

2 Experimental Section

2.1 Reagents and Instruments

Agar powder (mass fraction of ash ≤1.5%, biological grade), Shanghai Macklin Biochemical Co., Ltd.; *Acetobacter xylinum*, CGMCC 1.1812, Beijing Baocheng Biotechnology Co., Ltd.; ANF, Shanghai Xinchuang Houpu New Material Technology Co., Ltd.

Yeast extract, peptone, mannitol (mass fraction 99%), polyvinyl alcohol (PVA), tert-butanol, biological reagents; glucose monohydrate (mass fraction 99%), sodium citrate (mass fraction 99%), magnesium sulfate, sodium hydroxide, analytical grade, Shanghai Macklin Biochemical Co., Ltd.; deionized water, self-prepared.

The instrumentation employed in this work comprised a Spectrum One-B Fourier-transform infrared spectrometer (FTIR) from PerkinElmer (USA); a JSM-6460LV scanning electron microscope (SEM) from JEOL (Japan); a TriStar Ⅱ 3020 fully automated surface-area and pore-size analyzer (BET) from Micromeritics (USA); a D8 DISCOVER X-ray diffractometer (XRD) from Bruker (Germany); an LFY-606B limiting-oxygen-index tester from Shandong Textile Research Institute; a DRL-Ⅲ heat-flow thermal-conductivity tester from Xiangtan Instrument and Meter Co., Ltd.; and a YG(B)026HC-500 electronic fabric strength tester from Wenzhou Darong Textile Instrument Co., Ltd.

2.2 Methods

2.2.1 Preparation of Culture Medium

The liquid culture medium for Acetobacter xylinum was prepared by dissolving, one after another and with gentle addition, 15.0 g of glucose monohydrate, 3.0 g of yeast extract, 5.0 g of peptone, 0.5 g of sodium citrate, 1.0 g of magnesium sulfate, and 2.5 g of mannitol in 1 L of deionized water at 30 °C. Once all components had fully dissolved, the solution's pH was brought to 6 using 0.2 mol/L aqueous NaOH. The medium was then poured into a conical flask, sealed, and sterilized in a vertical pressure steam sterilizer at 120 °C for 30 min.

2.2.2 Preparation of BC Aerogel

Preparation of BC hydrogel: The conical flask containing 47 mL liquid culture medium for *Acetobacter xylinum* was transferred to an aseptic operating table for inoculation. 3 mL culture solution containing *Acetobacter xylinum* (a small amount of colony of purchased *Acetobacter xylinum* cultured in test tubes was picked and inoculated into liquid culture medium for *Acetobacter xylinum* to obtain the culture solution containing *Acetobacter xylinum*) was added into the above culture medium. The mixture was fully

shaken to separate the bacterial strains and make them fully dispersed in the liquid culture medium for *Acetobacter xylinum*. The mixture was placed in a biochemical incubator (30 ℃) for static in-situ culture for 5 d to obtain BC hydrogel.

Impurity removal: BC hydrogel was boiled and washed with 0.2 mol/L aqueous sodium hydroxide solution until it turned milky-white, then boiled and washed with deionized water for 2 h and allowed to stand for 20 min. The deionized-water washing process was repeated 2-3 times until neutrality was achieved, completing the impurity removal of BC hydrogel.

Solvent exchange: The impurity-removed BC hydrogel was soaked in 50 wt% tert-butanol aqueous solution and 100 wt% tert-butanol solution successively for 12 h each at 30 ℃, and then pre-cooled at −20 ℃ for 12 h.

Freeze-drying: After pre-cooling, freeze-drying was performed at −50 ℃ for 48 h to obtain BC aerogel. BC aerogel prepared by freeze-drying is a white, lightweight and water-absorbing porous material.

2.2.3 Preparation of BC/ANF Aerogel

First, 3 wt% PVA (based on the mass of liquid culture medium for *Acetobacter xylinum*) was added into 47 mL liquid culture medium for *Acetobacter xylinum*. Subsequently, ANF was added respectively at mass fractions of 0.5%, 1.0%, 2.5%, 5.0% and 7.5% relative to the liquid culture medium for *Acetobacter xylinum*. The mixture was stirred at 98 ℃ and then subjected to ultrasonic dispersion (70 W) for 30 min. Then the dispersion liquid was sterilized at 120 ℃ for 30 min. After sterilization, the conical flask was transferred to an aseptic operating table for inoculation. 3 mL culture solution containing *Acetobacter xylinum* was added into the above culture solution. The mixture was fully shaken to separate the bacterial strains and make them fully dispersed in the above dispersion liquid. The inoculated liquid culture medium was shaken on a shaker for 12 h to achieve uniform mixing of bacterial strains and dispersion liquid. It was then placed in a biochemical incubator (30 ℃) for static culture for 5 d to obtain BC/ANF hydrogels with different ANF contents. Afterwards, BC/ANF aerogels with different ANF contents were obtained through impurity removal, solvent exchange and freeze-drying processes (the same as Section 1.2.2), which were denoted as BC/ANF-0.5%, BC/ANF-1.0%, BC/ANF-2.5%, BC/ANF-5.0% and BC/ANF-7.5%, respectively.

2.3 Characterization and Testing

FTIR test: KBr tablet pressing method, wavenumber range 4000-400 cm^{-1}, resolution 4 cm^{-1}, scanning times 32 times. XRD analysis was performed with Cu Kα radiation (λ=0.1541 nm) at a tube voltage of 40 kV and a current of 40 mA, scanning from 5° to 60° at 8 (°)/min. For SEM imaging, the specimens were sputter-coated with gold and examined in low-energy secondary-electron (LEI) mode, with the working current set to 20 μA and the accelerating voltage to 5.0 kV. Specific surface area and pore-size distribution were derived from nitrogen adsorption–desorption isotherms recorded at 77.35 K on 0.0800 g of sample using the static adsorption method (BET). TGA measurements were conducted on 5–10 mg portions placed in crucibles, heated from ambient temperature to 600 °C at 20 °C/min under both nitrogen and air. For the limiting oxygen index (LOI) evaluation, the aerogels were sectioned into 60 mm × 50 mm × 2 mm specimens and tested with a limiting-oxygen-index apparatus to gauge flame retardancy. Thermal conductivity was determined by the heat-flow method, with specimen thickness first measured by vernier caliper and the instrument settings adjusted accordingly. Tensile behavior was assessed on an electronic fabric strength tester operated at a 50 N load and a crosshead speed of 100 mm/min.

3 Results and Discussion

3.1 Structural Characterization Analysis

Figure 1 shows the FTIR spectra of ANF, BC aerogel and BC/ANF-5.0%.

As shown in Figure 1, the absorption at 3341 cm^{-1} stems from —OH stretching, the band at 2919 cm^{-1} reflects asymmetric C—H stretching, and the intense signal at 1060 cm^{-1} arises from the skeletal vibration of the C—O—

C pyranose ring; these three features are characteristic of the BC aerogel. In addition, the band at 3328 cm^{-1} is attributed to N—H stretching within amide groups, while the absorptions at 1657 cm^{-1}, 1319 cm^{-1}, and 1518 cm^{-1} originate respectively from the C=O stretching, C—N stretching, and aromatic C—C vibrations of ANF[18].

In the FTIR spectrum of BC/ANF-5.0%, the peaks at 3328 cm^{-1}, 1657 cm^{-1}, 1518 cm^{-1} and 1319 cm^{-1} originate from ANF, and the peak at 1060 cm^{-1} comes from BC aerogel, indicating that BC/ANF-5.0% is a composite material composed of ANF and BC.

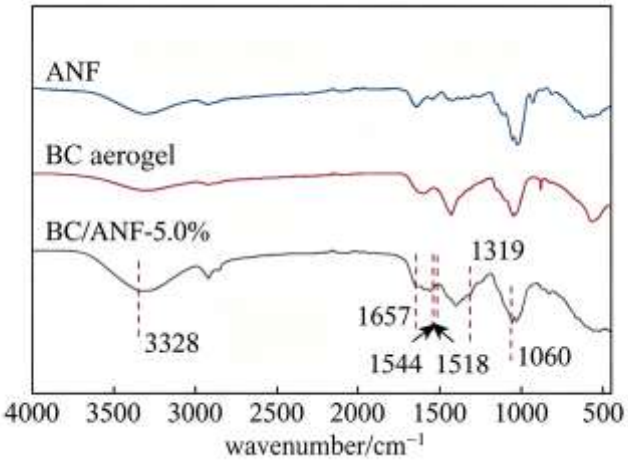

Figure 1 FTIR spectra of ANF, BC aerogel and BC/ANF-5.0%

Figure 2 displays the XRD patterns of BC aerogel and BC/ANF aerogels.

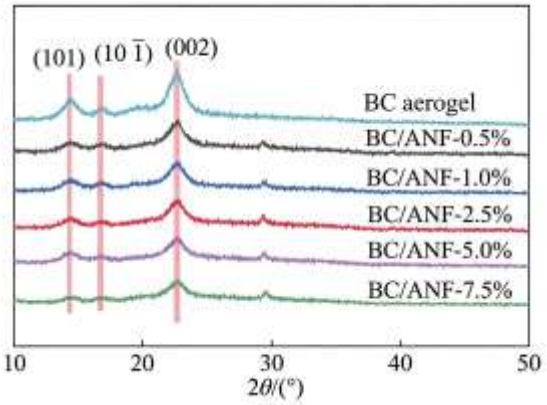

Figure 2 XRD patterns of BC aerogel and BC/ANF aerogels

Figure 2 presents the diffraction pattern of the BC aerogel, in which three well-resolved peaks at 2θ=14.6°, 16.9°, and 22.6° are indexed to the (101), (10\(\bar{1}\)), and (002) planes of the cellulose Ⅰ lattice[19], whereas the reflections emerging at 2θ=23.0° and 29.4° are assignable to the (200) and (004) planes[20]. BC/ANF aerogels show the diffraction peak of ANF at 2θ=29.4°. Compared with BC aerogel, BC/ANF-5.0% exhibits decreased diffraction-peak intensities at 2θ=14.6°, 16.9° and 22.6°, suggesting that the added ANF interferes with the growth of cellulose and the ordered arrangement of molecular chains.

3.2 Morphology Analysis

Figure 3 presents the SEM images of ANF, BC aerogel and BC/ANF aerogels.

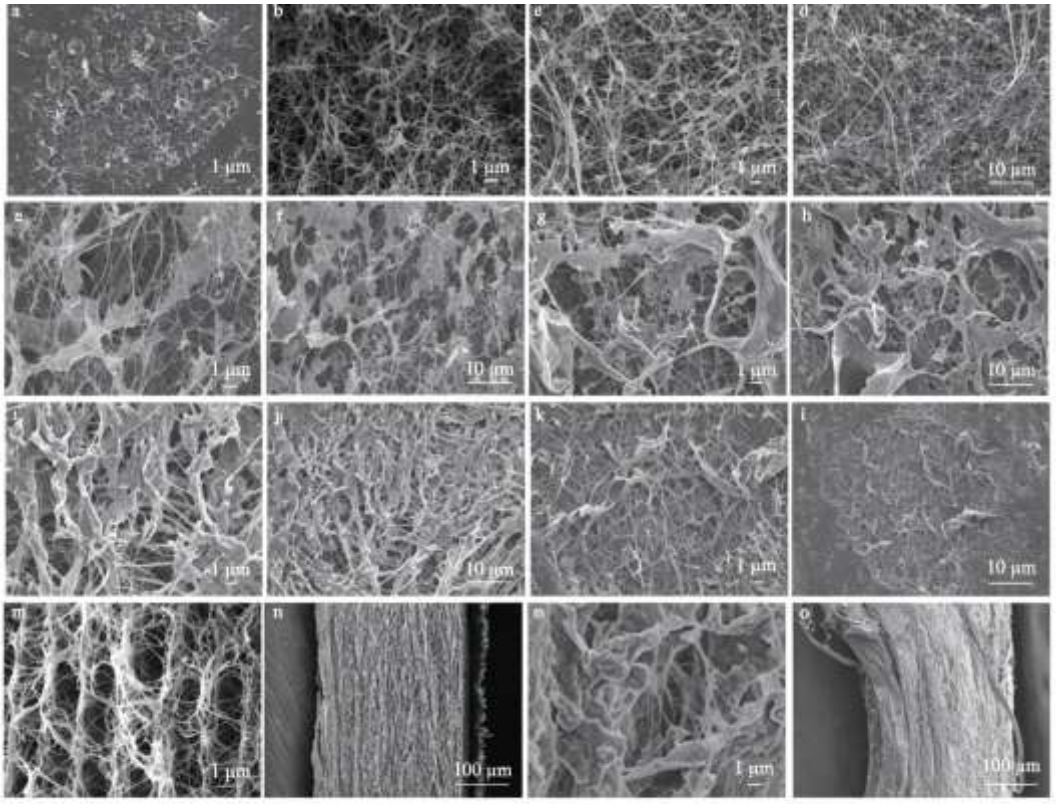

Figure 3 SEM images of ANF, BC aerogel and BC/ANF aerogels

Comparison of the micrographs in Figure 3 indicates that the ANF filaments (Figure 3a) are thicker than the fibrils constituting the BC aerogel (Figure 3b). The BC fibrils are interlaced into a random three-dimensional web (Figure 3b, m, n), and in cross-section the static layer-by-layer growth mode of BC yields an interconnected, porous lamellar architecture — the framework that accounts for the aerogel's overall morphology and porosity.

As more ANF is incorporated, the fibrillar network of the BC/ANF aerogel grows progressively more compact, and the adhesive features within it evolve from bead-shaped to thread-like morphologies (Figure 3c–j and Figure 3o, p). This is because part of BC grows attached to the surface of ANF, or BC microfibers interlace and entangle with ANF. Hydrogen bonds are formed between amide groups in ANF and hydroxyl groups in BC, enhancing the binding force between the two components and enabling effective stress transfer, so that the two components jointly resist external force under external load[21]. Due to physical entanglement and van der Waals forces generated when molecular chains come into close contact, the two components attract and approach each other, which facilitates the filling and winding of ANF in the BC fiber network. Under external force, it can hinder the relative sliding of fibers and share external load together, thus improving the mechanical properties of BC aerogel[22].

Figure 4 shows the nitrogen adsorption-desorption isotherms and pore-size distribution curves (inset) of BC aerogel and BC/ANF-5.0%. As can be seen from Figure 4, for BC aerogel and BC/ANF-5.0%, adsorption capacity increases at p/p_o<0.1, corresponding to micropore filling; adsorption capacity rises gradually at p/p_o=0.1-0.8, corresponding to mesopore filling; adsorption capacity increases rapidly when p/p_o≥0.8, which may be caused by capillary condensation. These features are consistent with type-Ⅳ isotherms. The inset pore-size distribution reveals that both BC aerogel and BC/ANF-5.0% possess pores falling within 4–20 nm, which further identifies them as mesoporous solids whose adsorption isotherms conform to type Ⅳ[23].

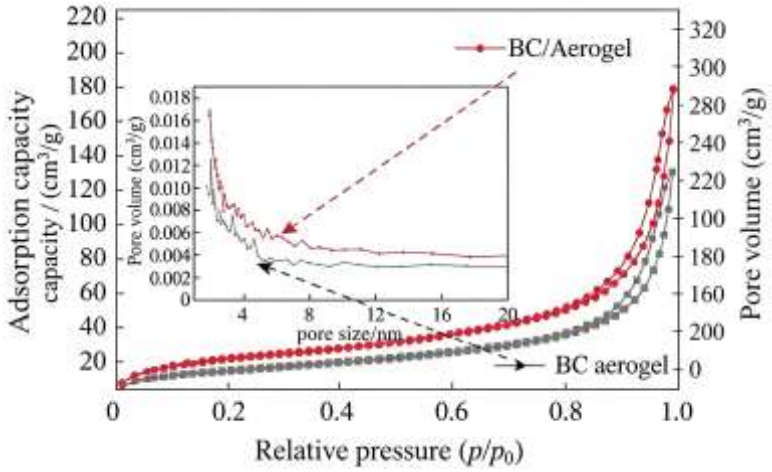

Figure 4 N2 adsorption-desorption isotherms and pore size distribution curves of BC aerogel and BC/ANF-5.0%

Measured specific surface areas are 55.0855 m²/g for the BC aerogel and 78.2688 m²/g for BC/ANF-5.0%, the latter exceeding the former by a factor of 1.42. Such a result demonstrates that BC/ANF-5.0% features a more highly developed pore network together with a greater surface area, a combination advantageous for enhanced thermal insulation.

3.3 Thermal-Performance Analysis

Figures 5 and 6 are the TG and DTG curves of ANF, BC aerogel and BC/ANF aerogels under nitrogen atmosphere, respectively.

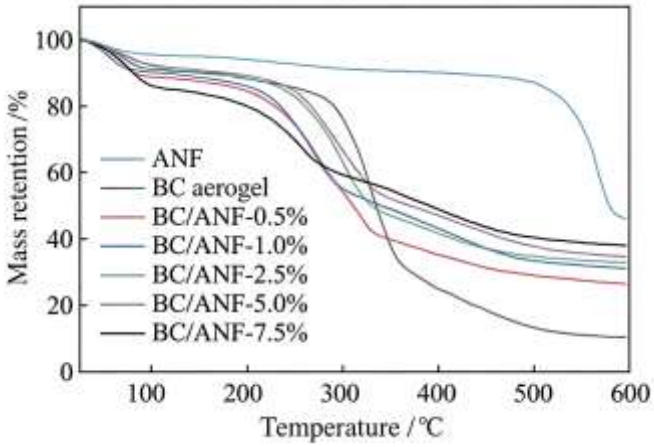

Figure 5 TG curves of ANF, BC aerogel and BC/ANF aerogels in N2

Figures 5 and 6 reveal that the early mass loss of the BC aerogel stems from the evaporation of water and residual small-molecule solvents[24]. Under nitrogen, the aerogel reaches its fastest decomposition at 340 °C and loses roughly 90% of its mass overall, whereas ANF does not decompose most rapidly until nearly 600 °C. As the ANF fraction rises, the BC/ANF aerogels exhibit progressively lower mass-loss rates and smaller total weight losses at every degradation stage. The total weight-loss ratio of BC/ANF-5.0% drops to approximately 65%. Compared with BC aerogel, the volatilization degree of small molecules such as water in BC/ANF aerogels decreases. The thermal-decomposition process within 120-300 ℃ does not change significantly, and the depolymerization of cellulose mainly occurs in this interval. The degree of thermal decomposition decreases greatly above 300 ℃, where the formation and decomposition of levoglucosan, dehydration and carbonization mainly take place[25]. This outcome confirms that integrating ANF with BC suppresses both the generation and the subsequent

breakdown of levoglucosan while accelerating char formation, thereby markedly enhancing the thermal stability of the BC aerogel.

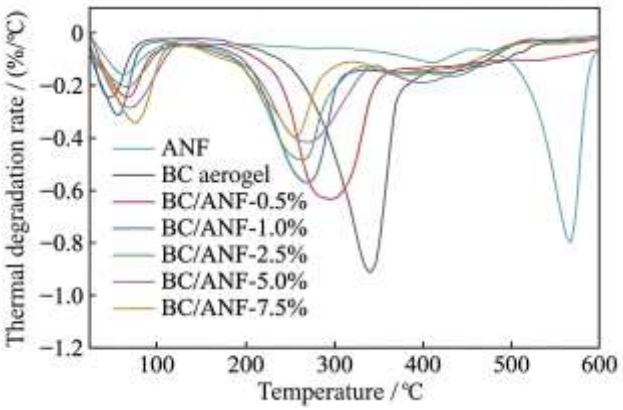

Figure 6 DTG curves of ANF, BC aerogel and BC/ANF aerogels in N2

Figures 7 and 8 are the TG and DTG curves of ANF, BC aerogel and BC/ANF aerogels under air atmosphere, respectively.

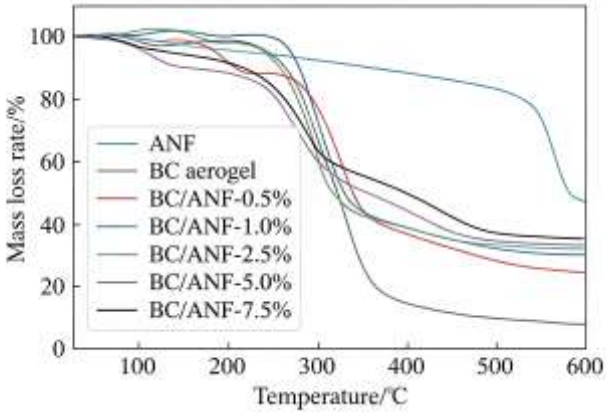

Figure 7 TG curves of ANF, BC aerogel and BC/ANF aerogels in air

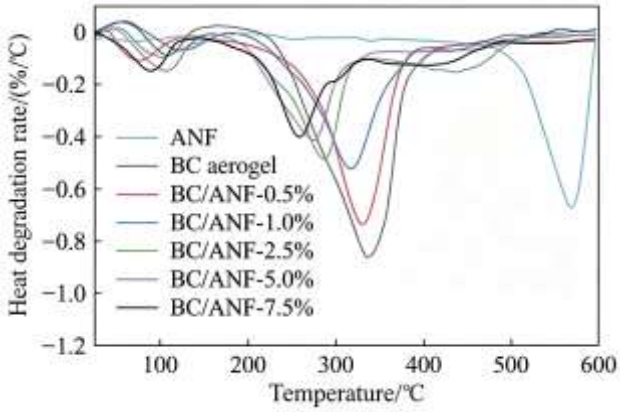

Figure 8 DTG curves of ANF, BC aerogel and BC/ANF aerogels in air

As shown in Figures 7 and 8, compared with the nitrogen atmosphere (Figures 5 and 6), the maximum decomposition temperature of BC aerogel in air drops to 334 ℃, and its final total weight-loss ratio rises to 92%.

The final total weight-loss ratio of BC/ANF-5.0% increases to 67%. Although the BC and BC/ANF aerogels lose marginally more mass when heated in air than in nitrogen, the difference between the two atmospheres remains minimal.

3.4 Flame-Retardant-Performance Analysis

The LOI data for the BC aerogel and the BC/ANF aerogels are compiled in Figure 9. Whereas the neat BC aerogel registers an LOI of 15.96%, the composite aerogels show a steady increase in LOI as the ANF fraction grows. The LOI value of BC/ANF-5.0% rises to 22.38%, and BC/ANF-7.5% achieves the highest LOI value of 23.74%. The significant increase in LOI indicates that ANF with flame-retardant function is embedded inside BC aerogel, endowing BC/ANF aerogel with relatively ideal flame-retardant performance.

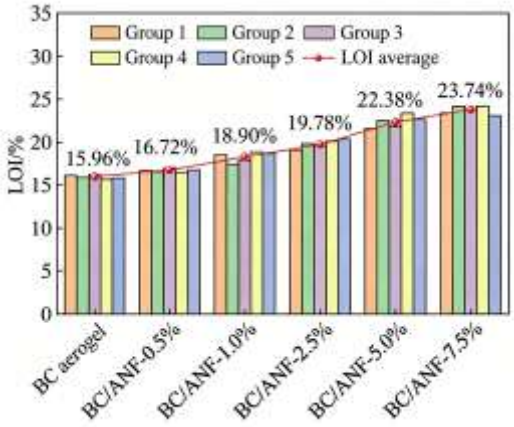

Figure 9 LOI of BC aerogel and BC/ANF aerogels

Figure 10 shows the SEM images of char residues after combustion of BC aerogel and BC/ANF-5.0%. It can be seen that BC aerogel produces fragile, powdery char residues after combustion (Figure 10a, b); the char-residue structure of BC/ANF-5.0% after combustion is relatively intact. This is because the addition of ANF promotes the carbonization of BC. ANF itself is also highly thermally stable; consequently, at elevated temperatures the BC/ANF aerogel develops a robust char layer that impedes the transport of heat, oxygen, and flammable volatiles, thereby strengthening its flame retardancy.

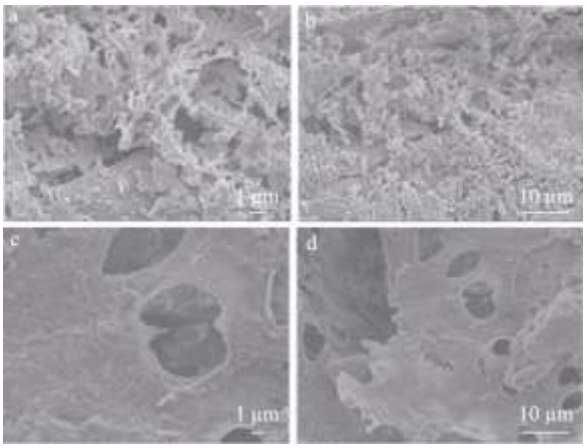

Figure 10 SEM images of the charred residues after combustion of BC aerogel (a, b) and BC/ANF-5.0% (c, d) at various magnifications

3.5 Thermal-Insulation-Performance Analysis

Figure 11 shows the thermal conductivity of BC aerogel and BC/ANF aerogels.

Figure 11 shows that the thermal conductivity of the BC/ANF aerogels declines progressively as more ANF is introduced: whereas the pure BC aerogel conducts heat at 0.0518 W/(m·K), the value for BC/ANF-5.0% falls to 0.0352 W/(m·K). This reduction arises because a higher ANF loading renders the pathways for heat conduction more tortuous, lowering the efficiency of heat transfer and hence improving the thermal insulation of the composite aerogel.

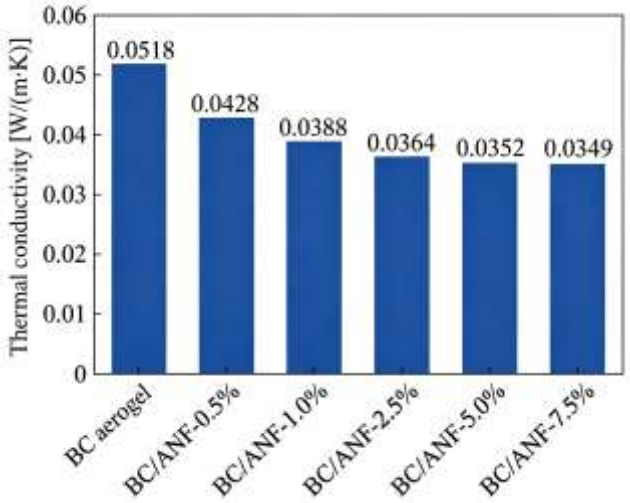

Figure 11 Thermal conductivity of BC aerogel and BC/ANF aerogels

Figure 12 compares the density and thermal conductivity of BC/ANF-5.0% with those of other common aerogel materials reported in recent years, such as polyimide, silica and graphene[26-39].

It can be observed from Figure 12 that BC/ANF-5.0% prepared in this work possesses favorable thermal-insulation performance. Nevertheless, BC composite aerogels with lower thermal conductivity (such as PI/BC aerogel) usually adopt special freeze-drying methods such as bidirectional freezing technology.

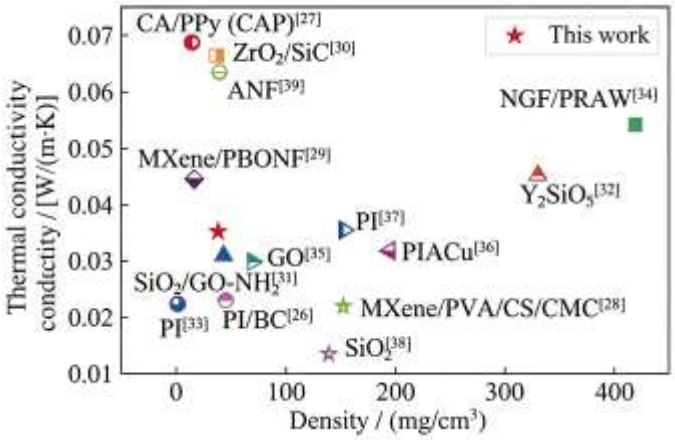

Figure 12 Comparison of thermal conductivity and density between BC/ANF-5.0% aerogel with other aerogels

Figure 13 shows the thermal conductivity of BC aerogel and BC/ANF-5.0% equilibrated for 24 h at 30 ℃ under different relative humidity.

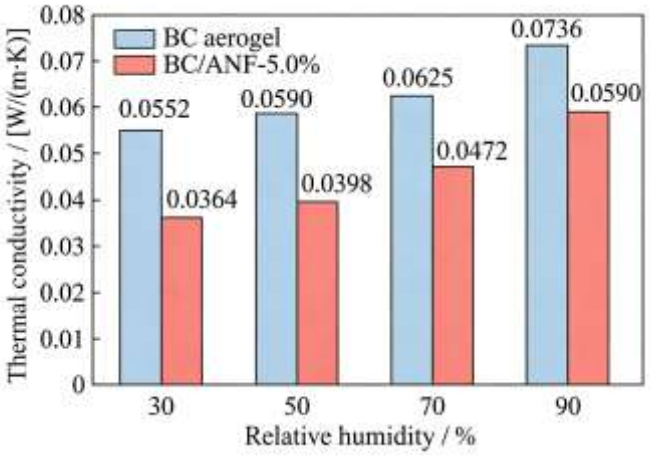

Figure 13 Thermal conductivity of BC aerogel and BC/ANF- 5.0% at different humidity

Figure 13 demonstrates that raising the ambient relative humidity drives up the thermal conductivity of both the BC aerogel and BC/ANF-5.0%. The underlying reason is that water, with its comparatively high conductivity of 0.5984 W/(m·K), is readily taken up from humid air by these porous materials through hydrogen bonding between moisture and the hydroxyl groups of BC. Specifically, as relative humidity climbs from 30% to 90%, the BC aerogel's conductivity grows from 0.0552 to 0.0736 W/(m·K), while that of BC/ANF-5.0% rises from 0.0364 to 0.0590 W/(m·K). Thus, despite the humidity-induced deterioration, BC/ANF-5.0% retains satisfactory thermal-insulation capability even at 90% relative humidity.

Figure 14 shows the temperature-variation curves of BC aerogel and BC/ANF-5.0% as functions of hot-stage temperature.

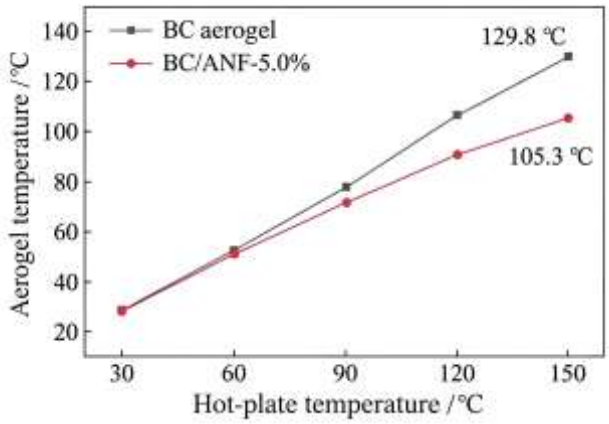

Figure 14 Temperature curves of BC aerogel and BC/ANF- 5.0% with temperature of hot stage

In the hot-stage heating experiment, the three-dimensional structure of aerogel exerts a remarkable effect on restricting heat conduction. It can be seen from Figure 14 that when the hot-stage temperature increases gradually from 30 ℃ to 150 ℃, the maximum temperature of BC aerogel reaches 129.8 ℃, while that of BC/ANF-5.0% is 105.3 ℃. It indicates that the three-dimensional nano-skeleton structures of the two aerogels can effectively increase heat-transfer paths and slow down heat conduction.

Figure 15 shows the temperature variation of BC/ANF-5.0% during repeated heating processes. According to Figure 15, the peak surface temperature attained by BC/ANF-5.0% is 105.5 °C during the initial heating cycle, climbing to 106.3 °C and 107.8 °C in the second and third cycles, respectively. Overall, the maximum

temperatures of the three heating cycles differ slightly. BC/ANF-5.0% exhibits good thermal stability during cyclic heating.

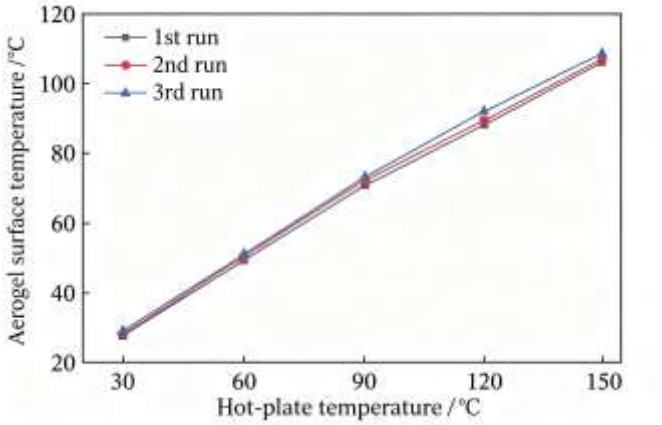

Figure 15 Cyclic heating curves of BC/ANF-5.0%

Taken together, BC/ANF-5.0% suppresses heat transport through its distinctive three-dimensional nanoarchitecture while maintaining dependable thermal behavior over repeated heating cycles — attributes that position it as a strong candidate for high-performance thermal-insulation applications.

3.6 Tensile-Performance Analysis

Figure 16 presents the physical photographs of BC/ANF hydrogel and BC/ANF-5.0%.

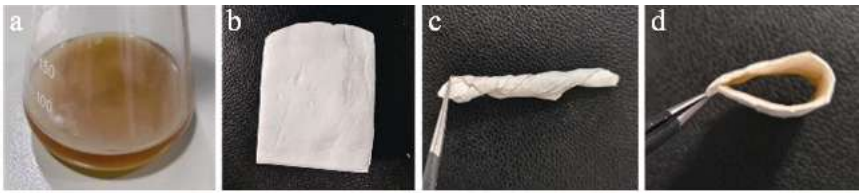

Figure 16 Physical photos of BC/ANF-5.0%

It can be seen from Figure 16 that BC/ANF hydrogel obtained by in-situ culture (Figure 16a), and BC/ANF-5.0% prepared by subsequent freeze-drying (Figure 16b), exhibit favorable structural integrity and flexibility under continuous twisting (Figure 16c) and bending (Figure 16d).

Figure 17 shows the stress-strain curves of BC aerogel and BC/ANF aerogels.

Figure 17 shows that the neat BC aerogel offers a tensile strength of 127.48 kPa and an elongation at break of 2.80%. As the ANF fraction rises, both parameters of the BC/ANF aerogels first climb and then fall, peaking at BC/ANF-5.0%, where the tensile strength reaches 946.13 kPa and the elongation at break 19.61% — improvements of 6.42- and 6.00-fold over the BC aerogel. This reinforcement stems from the in-situ compounding process, in which BC either grows directly on ANF surfaces or becomes entangled with the ANF filaments, yielding an integrated composite architecture. Beyond the optimum loading, however, surplus ANF tends to aggregate and interferes with BC growth, which undermines further gains in tensile performance.

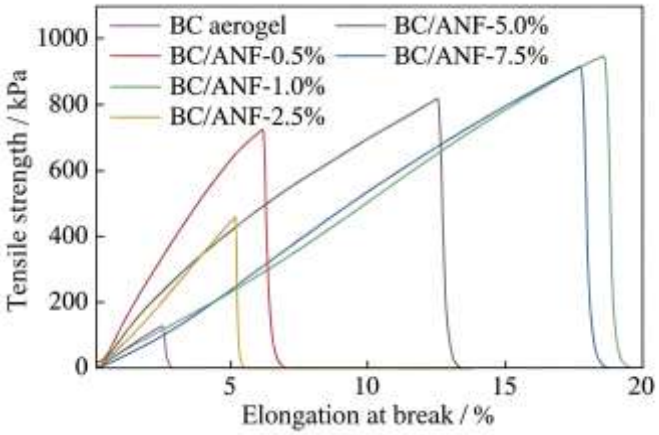

Figure 17 Stress-strain curves of BC aerogel and BC/ANF aerogels

4 Conclusions

BC/ANF aerogel was successfully prepared by adding ANF into culture medium containing *Acetobacter xylinum* for fermentation culture to realize in-situ compounding of BC and ANF, combined with freeze-drying technology.

Relative to the neat BC aerogel, BC/ANF-5.0% shows a reduction in nitrogen-atmosphere weight loss from 90% to 65%, an LOI improvement from 15.96% to 22.38%, an enlargement of specific surface area from 55.0855 m²/g to 78.2688 m²/g, a drop in thermal conductivity from 0.0518 W/(m·K) to 0.0352 W/(m·K), and tensile strength and elongation at break that are 6.42 and 6.00 times greater, respectively. Elevated ambient humidity does push the thermal conductivity of the composite aerogel upward to some degree; even so, at 90% relative humidity the conductivity of BC/ANF-5.0% climbs only to 0.0590 W/(m·K), leaving its insulating capability essentially intact.

Compared with pure BC aerogel, BC/ANF aerogel prepared in this work displays superior thermal stability, flame-retardant performance, thermal-insulation performance and tensile properties. It is expected to further broaden its application scope in thermal-management materials and smart wearable devices.

References

[1] HUANG Y, HUANG X Z, MA M T, et al. Recent advances on the bacterial cellulose-derived carbon aerogels [J]. Journal of Materials Chemistry C, 2021, 9(3): 818-828.

[2] ZHANG W J, XUE T, YIN Y J, et al. Preparation and performances of bacterial cellulose/thermoplastic polyu rethane composite aerogel fibers[J]. Fine Chemicals, 2024, 41(1): 114-120, 184.

[3] REVIN V V, PESTOV N A, SHCHANKIN M V, et al. A study of the physical and mechanical properties of aero gels obtained from bacterial cellulose[J]. Biomacromolecules, 2019, 20(3): 1401-1411.

[4] FLEURY B, ABRAHAM E, DE LA CRUZ J A, et al. Aerogel from sustainably grown bacterial cellulose pellicles as a thermally insulative film for building envelopes[J]. ACS Applied Materials & Interfaces, 2020, 12(30): 34115-34121.

[5] ZHANG W J, ZHAO G Z, WANG C X, et al. Core-shell bacterial cellulose/graphene oxide@polydopamine ae rogel fibers for personal thermal management textiles[J]. Macromolecular Chemistry and Physics, 2024, 2 25(14): 2300443.

[6] ZHENG X D, SUN W, ZHANG Y, et al. Bacterial cellulose nanofibrous ion imprinted aerogel for highly efficie nt recognition and adsorption of Dy(Ⅲ)[J]. Process Safety and Environmental Protection, 2022, 160: 70-7 9.

[7] LEI W, JIN D, LIU H P, et al. An overview of bacterial cellulose in flexible electrochemical energy storage[J]. ChemSusChem, 2020, 13(15): 3731-3753.

[8] HENSCHEN J, ILLERGÅRD J, LARSSON P A, et al. Contact-active antibacterial aerogels from cellulose nanofi brils[J]. Colloids and Surfaces B: Biointerfaces, 2016, 146: 415-422.
[9] LIU H Z, GENG B Y, CHEN Y F, et al. Review on the aerogel-type oil sorbents derived from nanocellulose[J]. ACS Sustainable Chemistry & Engineering, 2016, 5(1): 49-66.
[10] WICKLEIN B, ARRANZ J, MAYORAL A, et al. Nanostructured carbon-metal hybrid aerogels from bacterial ce llulose[J]. RSC Advances, 2017, 7(67): 42203-42210.
[11] ZHAO Y X, SUN B J, WANG T, et al. Synthesis of cellulose-silica nanocomposites by in situ biomineralizatio n during fermentation[J]. Cellulose, 2020, 27(2): 703-712.
[12] YANG B, WANG L, ZHANG M Y, et al. Fabrication, applications, and prospects of aramid nanofiber[J]. Adva nced Functional Materials, 2020, 30(22): 2000186.
[13] ZHAO Y, LI X, SHEN J N, et al. The potential of Kevlar aramid nanofiber composite membranes[J]. Journal o f Materials Chemistry A, 2020, 8(16): 7548-7568.
[14] WU Y D, WANG F, HUANG Y D, et al. Facile and simple fabrication of strong, transparent and flexible aram id nanofibers/bacterial cellulose nanocomposite membranes[J]. Composites Science and Technology, 201 8, 159: 70-76.
[15] CHEN S, WANG Y, FEI B, et al. Development of a flexible and highly sensitive pressure sensor based on an aramid nanofiber-reinforced bacterial cellulose nanocomposite membrane[J]. Chemical Engineering Journ al, 2022, 430: 131980.
[16] YANG Y, HUANG C H, GAO G, et al. Aramid nanofiber/bacterial cellulose composite separators for lithium-i on batteries[J]. Carbohydrate Polymers, 2020, 247: 116702.
[17] ZHANG S F, LUO J, ZHANG F J, et al. A porous, mechanically strong and thermally stable zeolitic imidazolat e framework-8@bacterial cellulose/aramid nanofibers composite separator for advanced lithium-ion batt eries[J]. Journal of Membrane Science, 2022, 652: 120461.
[18] YI X T, WANG F, WU Y D, et al. Aramid nanofibers/bacterial cellulose nanocomposite aerogels for high-effi cient cationic dye removal[J]. Materials Chemistry and Physics, 2021, 272: 124985.
[19] LI Z, WANG L, CHEN S, et al. Facilely green synthesis of silver nanoparticles into bacterial cellulose[J]. Cellu lose, 2015, 22(1): 373-383.
[20] GUAN Y, LI W, ZHANG Y L, et al. Aramid nanofibers and poly(vinyl alcohol) nanocomposites for ideal comb ination of strength and toughness via hydrogen bonding interactions[J]. Composites Science and Technolo gy, 2017, 144: 193-201.
[21] WANG S J, MENG W Y, WANG Z X, et al. Thermal insulating, light-weight and conductive cellulose/aramid nanofibers composite aerogel for pressure sensing[J]. Carbohydrate Polymers, 2021, 270: 118414.
[22] LI J Y, LU Z Q, XIE F, et al. Highly compressible, heat-insulating and self-extinguishing cellulose nanofiber/a ramid nanofiber nanocomposite foams[J]. Carbohydrate Polymers, 2021, 261: 117837.
[23] CUI W Q, SHAN X Y, CAI W J, et al. Architectural design of a multichannel porous carbon fiber for efficient electromagnetic microwave absorption[J]. Langmuir, 2024, 40(42): 22290-22299.
[24] IZAKURA S, KOGA H, UETANI K, et al. Humidity-responsive thermal conduction properties of bacterial cell ulose films[J]. Cellulose, 2021, 28(9): 5363-5372.
[25] KAWAMOTO H. Reactions and molecular mechanisms of cellulose pyrolysis[J]. Mokuzai Gakkaishi, 2015, 6 1(1): 1-24.
[26] ZHANG X, ZHAO X Y, XUE T T, et al. Bidirectional anisotropic polyimide/bacterial cellulose aerogels by free ze-drying for super-thermal insulation[J]. Chemical Engineering Journal, 2020, 385: 123963.
[27] WANG S J, MENG W Y, LYU H F, et al. Thermal insulating, light-weight and conductive cellulose/aramid na nofibers composite aerogel for pressure sensing[J]. Carbohydrate Polymers, 2021, 270: 118414.
[28] SUN Q, ZHANG X Y, GU P Z, et al. Highly stretchable mxene-based meta-aerogels with near-zero and nega tive poisson's ratios[J]. Advanced Functional Materials, 2024, 34(7): 2308537.
[29] WU Z H, FENG X L, QU Y X, et al. Silane modified MXene/polybenzazole nanocomposite aerogels with exc eptional surface hydrophobicity, flame retardance and thermal insulation[J]. Composites Communication s, 2023, 37: 101402.
[30] LIU F Q, HE C B, JIANG Y G, et al. Ultralight ceramic fiber aerogel for high-temperature thermal superinsul ation[J]. Nanomaterials, 2023, 13: 1305.
[31] XIONG L Y, ZHENG W J, CAO S L, et al. Organic-inorganic double-gel system thermally insulating and hydro phobic polyimide aerogel[J]. Polymers, 2022, 14(14): 2818.
[32] GU H T, HOU X B, ZHANG B, et al. Novel high-temperature-resistant Y_2SiO_5 aerogel with ultralow thermal conductivity[J]. International Journal of Applied Ceramic Technology, 2019, 16(6): 2393-2397.

[33] WANG S, DING R D, LIANG G Q, et al. Direct synthesis of polyimide curly nanofibrous aerogels for high-performance thermal insulation under extreme temperature[J]. Advanced Materials, 2024, 36(13): 2313444.
[34] WU C, WANG L M, YAN X J, et al. Environmental-friendly and fast production of ultra-strong phenolic aerogel composite with superior thermal insulation and ablative-resistance[J]. Composites Science and Technology, 2024, 256: 110776.
[35] YUE C W, FENG J, JIANG Y G, et al. Thermal conductivity of aerogel composites with oriented nitrogen-doped graphene[J]. Composites Science and Technology, 2017, 146: 198-202.
[36] LI D D, YE Q B, ZHAO D, et al. Construction of polyimide composite aerogels via multi-coordination structure of polymer-metal for improving heat-induced shrinkage, thermal insulation, mechanical and dielectric properties[J]. Materials Today Communications, 2024, 39: 109035.
[37] LI D D, LU Z H, KE Z, et al. Moisture resistant polyimide aerogel membranes with low dielectric constant and super thermal insulation for electronic device under harsh environment[J]. Polymer, 2024, 290: 126478.
[38] REZAEI E, MOGHADDAS J. Thermal conductivities of silica aerogel composite insulating material[J]. Advanced Materials Letters, 2016, 7(4): 296-301.
[39] PENG H, QIN W F, LI G, et al. An efficient fabrication method of lightweight aramid nanofibrous aerogels for high-efficient sound absorption and thermal properties[J]. Journal of Physics D: Applied Physics, 2024, 57(14): 145402.